A Robust Method for Filling the Gaps in MODIS and VIIRS Land Surface Temperature Data

Rui Yao, Lunche Wang, Xin Huang, *Senior Member, IEEE*, Liang Sun, Ruiqing Chen, Xiaojun Wu, Wei Zhang, and Zigeng Niu

***Abstract*— Satellite-derived land surface temperatures (LSTs) are a critical parameter in various fields. Unfortunately, there are numerous gaps in LST products due to cloud contamination and orbital gaps. In previous studies, various gapfilling methods have been developed. However, most of those methods use only spatiotemporal information to fill gaps. In this study, a gapfilling method called the enhanced hybrid (EH) method that integrates spatiotemporal information and information from other similar LST products was proposed. The accuracy of the EH method was compared with the accuracies of three other gapfilling methods that only use spatiotemporal information: Remotely Sensed DAily land Surface Temperature reconstruction (RSDAST), interpolation of the mean anomalies (IMAs), and Gapfill. It was found that the correlations between the four LST products were strong, indicating that using information from other products may improve the accuracy of gapfilling. On average, the mean absolute errors (MAEs) of the data filled using the EH method were 23.7%–52.7% lower than those of RSDAST, 35.4%–38.7% lower than those of IMA, and 38.5%–46.9% lower than those of the Gapfill method. The usage of information from other similar LST products was the main reason for the high accuracy observed for the EH method. In addition, the LST images filled using the RSDAST and IMA methods had some outliers, while there were fewer obvious outliers in the LST images filled with the EH method. It was concluded that the EH method is a robust gapfilling method with a high accuracy.**

***Index Terms*— China, gapfilling, land surface temperature (LST), remote sensing, interpolation.**

Manuscript received August 28, 2020; revised October 30, 2020, November 26, 2020, and December 23, 2020; accepted January 18, 2021. This work was supported in part by the National Natural Science Foundation of China under Grant 41771360, Grant 41975044, Grant 41801021, Grant 41905032, Grant 42001314, and Grant 42001016; and in part by the Fundamental Research Funds for National Universities, China University of Geosciences (Wuhan). *(Corresponding author: Lunche Wang.)*

Rui Yao, Lunche Wang, Xiaojun Wu, Wei Zhang, and Zigeng Niu are with the Hubei Key Laboratory of Critical Zone Evolution, School of Geography and Information Engineering, China University of Geosciences, Wuhan 430074, China (e-mail: yaorui123@cug.edu.cn; wang@cug.edu.cn; 1748287529@qq.com; 975824163@qq.com; 1164645120@qq.com).

Xin Huang is with the School of Remote Sensing and Information Engineering, Wuhan University, Wuhan 430079, China, and also with the State Key Laboratory of Information Engineering in Surveying, Mapping and Remote Sensing, Wuhan University, Wuhan 430079, China (e-mail: huang_whu@163.com).

Liang Sun and Ruiqing Chen are with the Institute of Agricultural Resources and Regional Planning, Chinese Academy of Agricultural Sciences/Key Laboratory of Agricultural Remote Sensing, Ministry of Agriculture, Beijing 100081, China (e-mail: sunliang@caas.cn; chenrq@mails.ccnu.edu.cn)

This article has supplementary material provided by the authors and color versions of one or more figures available at https://doi.org/10.1109/TGRS.2021.3053284.

Digital Object Identifier 10.1109/TGRS.2021.3053284

I. Introduction

LAND surface temperature (LST) represents the temperature of the earth's surface, which plays an important role in many research fields. For example, it can be used to investigate urbanization and the urban heat island effect [1], [2], estimate air temperature and soil moisture [3]–[5], and study climate warming and natural disasters [6], [7].

Satellite remote sensing is an effective way to obtain LSTs. The Moderate Resolution Imaging Spectroradiometer (MODIS) and Visible Infrared Imaging Radiometer Suite (VIIRS) provide two excellent satellite-derived LST products that have global coverage and high temporal resolutions. However, MODIS and VIIRS LST data have numerous gaps, mainly due to cloud contamination and orbital gaps. For example, Li *et al.* [8] found that the proportion of valid data to total data in MODIS LST products was only approximately 28% in urban areas of the conterminous United States. Gaps in LST products seriously limit their application. For instance, eight-day composite LST data were averaged into monthly and seasonal composites with which to study the urban heat island effect [9]–[11]. In this averaging process, only valid LSTs were used, which caused some uncertainty [12]. In addition, air temperature data estimated with LST data have many gaps due to the gaps in the LST data [13]–[16]. For example, Zhang *et al.* [13] estimated the daily air temperature on the Tibetan Plateau from 2003 to 2010. A total of four LST variables (MOD11A1 daytime and nighttime LSTs, and MYD11A1 daytime and nighttime LSTs) were used to reduce the missing values in the estimated air temperature data. However, 14% of the values were still missing in the final air temperature maps.

To solve this problem, various methods for reconstructing missing LST data have been developed. These methods can generally be divided into two types: 1) the reconstruction of clear-sky LSTs, in which unreal LSTs are reconstructed, assuming that there are no cloud effects [8], [17]–[21] and 2) the reconstruction of cloudy-sky LST, in which real LSTs are constructed under cloudy-sky conditions [22]–[27]. The reconstructed clear-sky LST data have successfully been used to analyze the surface urban heat island effect [28], investigate the relationship between LSTs and vegetation coverage [29], estimate air temperature [30], [31], calculate the dryness index, and support drought risk management [32]. In addition, the

estimation of clear-sky LSTs is an important step in some methods for estimating cloudy-sky LSTs [23], [33], [34]. For example, Zeng *et al.* [23] first reconstructed clear-sky LSTs for cloudy regions and then corrected the clear-sky LSTs to cloudy-sky LSTs. Wang *et al.* [34] divided cloudy pixels into two categories: cloud shadows and illuminated surfaces. The illuminated surfaces were filled with clear-sky LSTs. Therefore, the present study will focus on the reconstruction of clear-sky LSTs.

The data–model fusion method (data and model represent remotely sensed LST and land surface model-based LST, respectively) [35], surface energy balance model [23], and passive microwave data [25] can be used to reconstruct cloudy-sky LSTs. The methods for reconstructing clear-sky LSTs can normally be grouped into four categories: 1) the use of spatial information to fill the gaps (i.e., spatial gapfilling) [36]–[38]. Spatial gapfilling assumes that the LST of a given pixel will be more strongly correlated with the LSTs of pixels that are closer to that pixel than those that are farther away. 2) The use of temporal information to fill the gaps (i.e., temporal gapfilling) [29], [39]. Temporal gapfilling is based on the hypothesis that LSTs on a given day will have stronger relationships with the LSTs of closer days than with the LSTs of days that are further away. 3) The use of information from another similar LST product to fill the gaps [40], [41]. These methods use the information from the MOD11A1 LST product to fill the gaps in MYD11A1 data because these two data sets have similar monitoring times and the same spatiotemporal resolution. 4) The hybrid method [8], [17]–[20], [42], [43], which simultaneously uses at least two kinds of information to fill the gaps in LST data. Hybrid methods that use spatiotemporal information to fill gaps (i.e., spatiotemporal gapfilling) have been widely developed [17]–[20], [33], [42]–[44]. Spatiotemporal gapfilling generally has a higher accuracy than spatial gapfilling or temporal gapfilling do because it uses more information [8], [17], [42]. However, to our knowledge, few studies have integrated these three kinds of information (i.e., spatial, temporal, and other similar LST products) to fill the gaps in LST data. Li *et al.* [8] developed a hybrid method that uses three kinds of information to fill the gaps in MYD11A1 LST data. However, this method first fills approximately half of the gaps using temporal information and the MOD11A1 LST product and then fills the remaining gaps using spatiotemporal information. Therefore, these three kinds of information were not fully used by the method developed by Li *et al.* [8]. A comparison study showed that the accuracy of this method was lower than that of the spatiotemporal gapfilling method [33].

This study aims to develop a method [called the enhanced hybrid (EH) method] that integrates spatiotemporal information and information from other similar LST products to reconstruct clear-sky LSTs. The novel element of this method is that it makes full use of three kinds of information. This is different from all previous articles. In the following text, Section II presents the study areas and data. Section III shows the gapfilling method developed in this study. Sections IV and V show the results and discussions, respectively. Section VI summarizes this study.

II. Study Areas and Data

A. Study Areas

The study areas in this study include two regions in China: 1) the Beijing–Tianjin–Hebei region (BTH) and 2) the Pearl River Delta region (PRD) (Fig. 1). These two regions have distinct geographical locations and climate types that were used to test the universality of the gapfilling method.

The BTH region includes Beijing city, Tianjin city, and Hebei Province (Fig. 1). It covers an area of approximately 218 000 km^2 and has a population of approximately 110 million. The altitude of BTH generally decreases from northwest to southeast, ranging from below sea level to over 2600 m (Fig. 1). This region is characterized by a warm temperate monsoon climate, with an average annual mean air temperature (MAT) of 11.4 °C and an average annual total precipitation of 547 mm.

The PRD region includes Guangdong Province and the Hong Kong Special Administrative Region. The PRD area is approximately 180 800 $km^{2,}$ and the population is approximately 120 million. The elevation gradually decreases from north to south. The PRD region is characterized by a subtropical monsoon climate, with an average annual MAT of 22.3 °C and an average annual total precipitation of 1761 mm.

B. Data

A total of four LST products were used in the present study. MODIS MOD11A1 (monitored at 10:30 am and pm local solar time) and MYD11A1 (monitored at 1:30 am and pm local solar time) daily daytime and nighttime LST products with a 1-km spatial resolution in 2018 were used. The LST data of these products are retrieved using a split-window (SW) algorithm [45], [46]. In 2018, the National Aeronautics and Space Administration (NASA) released new MODIS (MOD21 and MYD21) and VIIRS (VNP21, monitored at 1:30 am and pm local solar time) LST products with a 1-km spatial resolution. The LST data are retrieved using a temperature emissivity separation (TES) algorithm in these products [47]. MODIS MYD21A1 (including MYD21A1D and MYD21A1N) and VIIRS VNP21A1 (including VNP21A1D and VNP21A1N) daily LST data in 2018 were also used in this study. To our knowledge, MYD21A1 and VNP21A1 have only been used by few previous studies since these data were released recently. The MODIS MOD21A1 TES data were not used, as these data were only available from 2001 to 2008. The VIIRS SW data were not used since daily composite data were not available. The MOD11A1, MYD11A1, MYD21A1, and VNP21A1 products are abbreviated as MOD11, MYD11, MYD21, and VNP21, respectively, in the following text.

III. Methods

A. Gapfilling Method Developed in This Study

In the present study, a gapfilling algorithm called EH was proposed to reconstruct the missing LSTs. Daytime and nighttime LST data were processed separately. The EH method includes the following five steps. A schematic of the EH method is shown in Fig. 2.

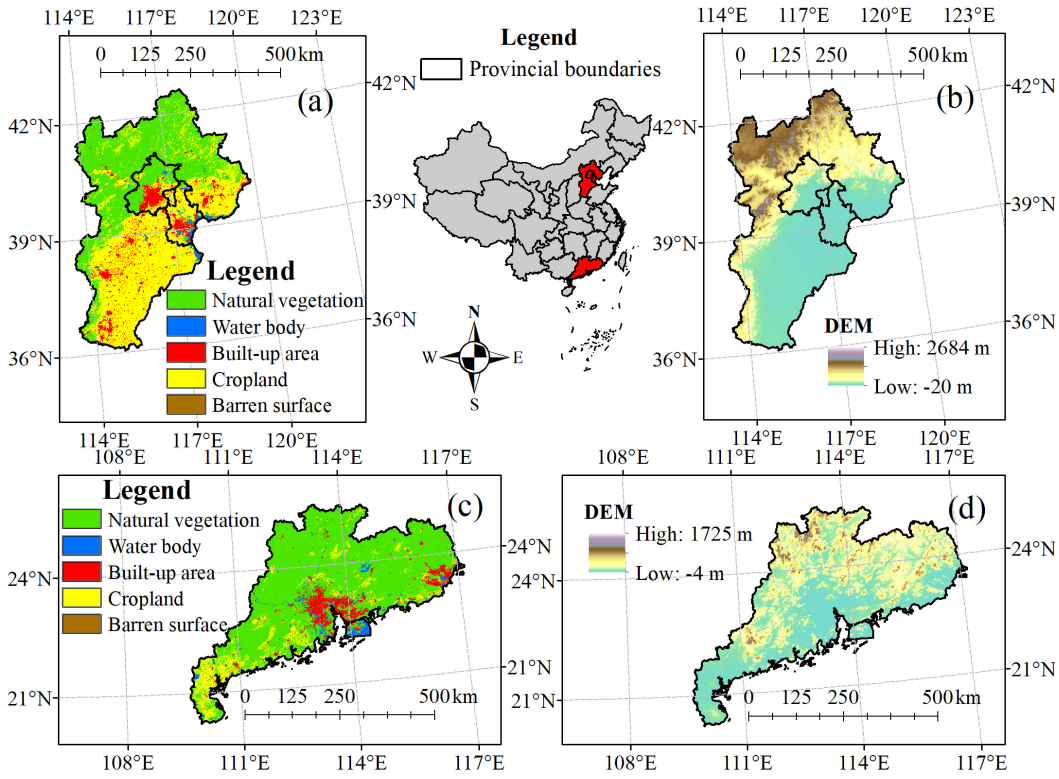

Fig. 1. Study areas. (a) Land cover map of the BTH region. (b) Elevation map of BTH. (c) Land cover map of the PRD region. (d) Elevation map of PRD.

1) The outliers in the LST data were removed. Satellite-derived LST data have some outliers primarily due to undetected clouds [48] and incorrect emissivity estimations [49]; these outliers are especially seen in the MYD21 LST data [49]. The undetected clouds occur under cloudy-sky conditions, but incorrect estimations of emissivity occur under clear-sky conditions. In BTH, if the daytime (nighttime) LST of a pixel was over 15 °C (12 °C) higher or lower than the mean daytime (nighttime) LST of the preceding and following ten days at the same pixel of the same product, it was considered an outlier. In this process, missing values were not used to calculate mean LSTs. For example, if there were 12 valid and 8 missing values for a pixel, the mean of the pixel was calculated using the 12 valid values. The number of preceding and following days was set as 15 in PRD because there were more missing values in the LST products for the PRD region. These outliers were also considered gaps in the following steps. This step can be expressed as follows:

$$\mathrm{LST}_s = \begin{cases} \mathrm{LST}_s, & \text{if } \mathrm{LST}_{\mathrm{mean},s} - t < \mathrm{LST}_s \\ & < \mathrm{LST}_{\mathrm{mean},s} + t \\ \text{missing value}, & \text{otherwise} \end{cases} \quad (1)$$

where LST_s is the LST of pixel s; $\mathrm{LST}_{\mathrm{mean},s}$ represents the mean LST of the preceding and following ten (or 15) days at pixel s, and t is set to 15 °C and 12 °C for daytime and nighttime, respectively.

2) A subset of LST images were defined for the target image (the image to be filled). These images were used to fill the gaps in the target image. The subset consisted of 11 images: a) three other LST products for the same day as that of the target image (three images) and b) the same product as that of the target image from the preceding and following four days (eight images). It can be seen that this subset contains information from other LST products. An example is shown in Fig. 2. The number of preceding and following days was selected as four because this number was selected by previous studies [8], [19], [42].

3) Spatial windows for the target pixel (the pixel to be filled) were defined. For the target pixel, a 21 × 21-km window [8], [42], centered on the target pixel, was first generated. If there were at least five valid pixels in the window in the target image, this window was selected for the target pixel. If this requirement was not met, the size of the spatial window iteratively increased with an interval of 20 km (i.e., to 41 × 41 km, 61 × 61 km, etc.) until this requirement was met. We set the maximum window size to 201 × 201 km because: a) filling missing LSTs using a large window requires considerable computing time [18] and b) the accuracy of the spatiotemporal gapfilling method is lower than that of the temporal gapfilling method when the size of the gap is large enough [27]. After that, the LSTs of the pixels in the windows in the subset of images were extracted (Fig. 2). These LSTs were defined as the prediction set (except for that of the target pixel itself).

4) The target pixel was predicted. The prediction set was further divided into three groups: a) LSTs of the pixels

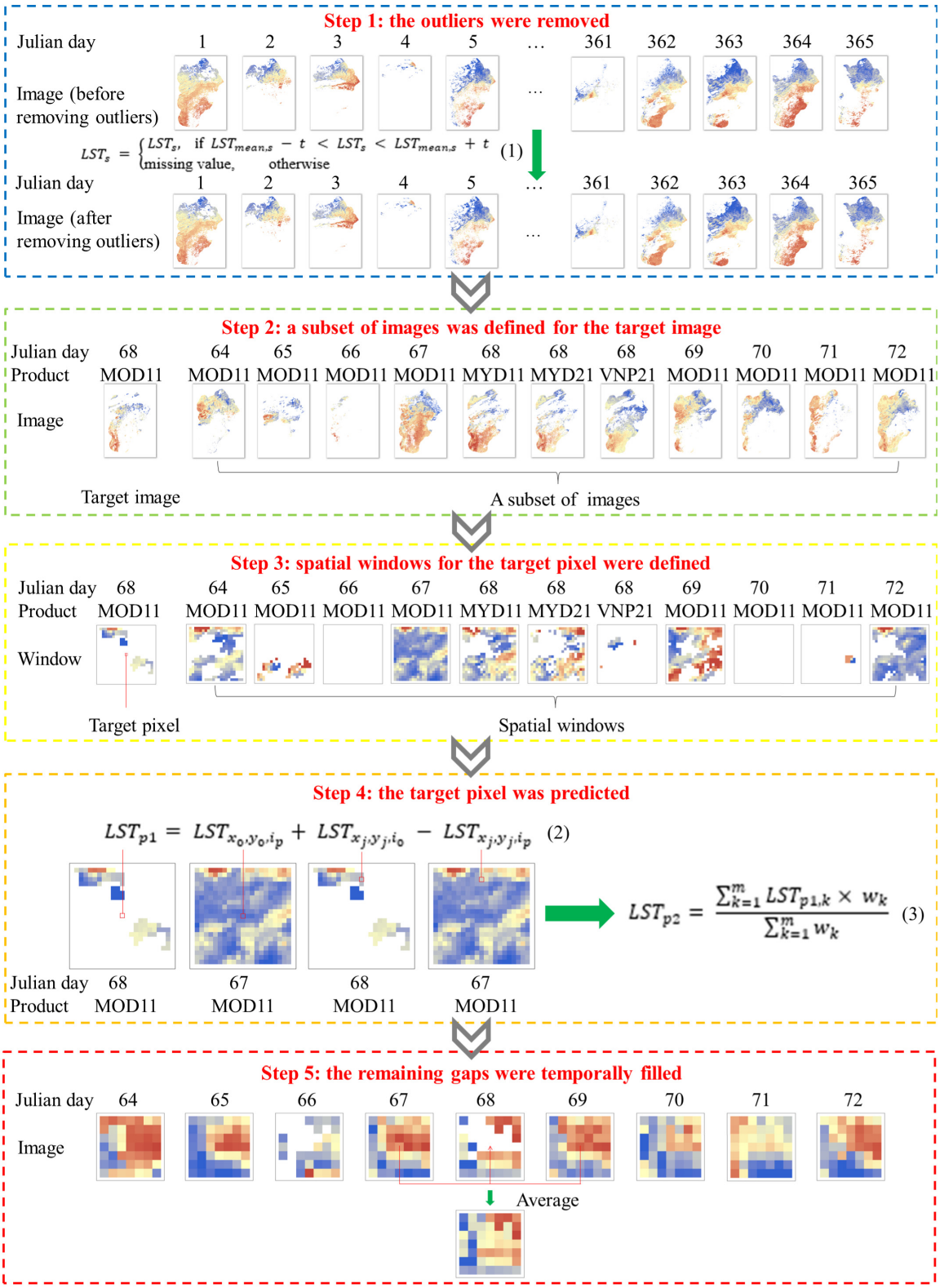

Fig. 2. Schematic of the EH method. MOD11 daytime LST data on March 9, 2018, were used as examples (target image). The MOD11A1, MYD11A1, MYD21A1, and VNP21A1 products are abbreviated as MOD11, MYD11, MYD21, and VNP21, respectively.

at the same location (but from different images) as the target pixel; b) LSTs of the pixels in the same image (but at different locations) as the target pixel; and c) LSTs of other pixels. The prediction set includes three kinds of information: group a) includes temporal information and information from other similar LST products; group b) includes spatial information; and group c) includes three kinds of information. Then, the LST of the target pixel

can be predicted using (2), which simultaneously uses three kinds of information

$$\mathrm{LST}_{p1}=\mathrm{LST}_{x_0,y_0,i_p}+\mathrm{LST}_{x_j,y_j,i_0}-\mathrm{LST}_{x_j,y_j,i_p} \tag{2}$$

where LST_{p1} is the predicted LST of the target pixel; (x_0, y_0) is the location of the target pixel; i_0 is the target image; $\mathrm{LST}_{x_0,y_0,i_p}$ is the LST at location (x_0, y_0) in image i_p, which is an image in the subset; $\mathrm{LST}_{x_0,y_0,i_p}$ belongs to group (a); $\mathrm{LST}_{x_j,y_j,i_0}$ is the LST at location (x_j, y_j) in the target image; (x_j, y_j) is a location in the spatial window; $\mathrm{LST}_{x_j,y_j,i_0}$ belongs to group (b); $\mathrm{LST}_{x_j,y_j,i_p}$ is the LST at location (x_j, y_j) in image p; and (x_j, y_j, i_p) belongs to group (c). This equation was proposed by Sun *et al.* [19] and was based on the hypothesis that the LST difference between two days (or images) of a pixel will be similar to that of a nearby pixel

$$\mathrm{LST}_{p1}-\mathrm{LST}_{x_0,y_0,i_p}=\mathrm{LST}_{x_j,y_j,i_0}-\mathrm{LST}_{x_j,y_j,i_p} \tag{3}$$

where, if $\mathrm{LST}_{x_0,y_0,i_p}$ is placed on the right of the equal sign, (3) becomes (2). Note that the LST cannot be predicted when at least one of the variables on the right side of the equal sign in (2) is missing. Because the LST of the target pixel may be predicted using many pixels in the prediction set, the LST of the target pixel was finally predicted as the weighted average of these predicted values

$$\mathrm{LST}_{p2}=\frac{\sum_{k=1}^{m}\mathrm{LST}_{p1,k}\times w_k}{\sum_{k=1}^{m} w_k} \tag{4}$$

where LST_{p2} is the final predicted LST for the target pixel; m is the total number of LSTs that were predicted using the prediction set and (2); $\mathrm{LST}_{p1,k}$ is the kth predicted LST; and w_k is the weight of the kth predicted LST. The weight, w_k, was calculated using three indexes

$$w_k=\frac{1}{\mathrm{DI}_k\times\mathrm{SI}_k\times\mathrm{SDI}_k} \tag{5}$$

where the distance index (DI) was calculated as:

$$\mathrm{DI}_k=\sqrt{(x_0-x_k)^2+(y_0-y_k)^2} \tag{6}$$

where (x_0, y_0) is the location of the target pixel and (x_k, y_k) is the location of the pixel in the prediction set for the kth predicted LST. The reason for using DI is that a given pixel generally has stronger correlations with closer pixels than with pixels that are farther away. The similarity index (SI) was calculated as

$$\mathrm{SI}_k=|\mathrm{LST}_{x_0,y_0,i_q}-\mathrm{LST}_{x_k,y_k,i_q}|+1 \tag{7}$$

where $\mathrm{LST}_{x_0,y_0,i_q}$ is the pixel at location (x_0, y_0) (the location of the target pixel) in image i_q, which is an image in subset; $\mathrm{LST}_{x_0,y_0,i_q}$ belongs to group (a); $\mathrm{LST}_{x_k,y_k,i_q}$ is the LST of the pixel at location (x_k, y_k) in image i_q; and $\mathrm{LST}_{x_k,y_k,i_q}$ belongs to group (c). The reason for using SI is that a given pixel generally has similar surface characteristics (e.g., land cover and elevation) as pixels that have similar LSTs. Finally, the subset includes images from other similar LST products and from near days, and these images may have different degrees of correlations with the target image. Therefore, a standard deviation index (SDI) was used to weight each image. The SDI was calculated as the spatial standard deviation of the LST difference between the target image and image q

$$\mathrm{SDI}_k=\sqrt{\frac{1}{n}\times\sum_{r=1}^{n}\left(\mathrm{LSTD}_{q,r}-\overline{\mathrm{LSTD}_q}\right)^2} \tag{8}$$

where n is the number of pixels for which both the target image and image q have valid LSTs; $\mathrm{LSTD}_{q,r}$ is the LST difference between the target image and image q at the rth pixel; and $\overline{\mathrm{LSTD}_q}$ is the average LST difference between the target image and image q. The reason for using SDI is as follows. If the spatial standard deviation of the LST difference between the target image and a given image in the subset was low, the LST difference between the target image and this image would be stable across the whole image. The prediction of missing LSTs using samples from this image will have high accuracy because the hypothesis of gapfilling is that the LST difference between two images of a given pixel will be similar to that of a nearby pixel. Therefore, when the spatial standard deviation of the LST difference between the target image and an image in the subset is low, a high weight should be set.

5) The remaining gaps were temporally filled. There were still some gaps in the target image that were not filled with the above-mentioned steps. These gaps occurred: a) when the whole target image was empty; b) when the LSTs were missing for a pixel in the target image and in all 11 images in the subset; and c) when the size of the gap was large. For the first case, temporal gapfilling is the only choice to fill the gaps because there is no spatial information to use. Therefore, a simple temporal interpolation method was used to fill the remaining gaps. Specifically, the missing values were filled using valid LSTs measured on the nearest dates at the same pixel. If the missing values could be filled using valid LSTs from two equally nearby dates, the average of the two valid values was used. This step can be expressed as follows:

$$\mathrm{LST}_{p3}=\begin{cases}\mathrm{LST}_{x_0,y_0,t1}, & \text{if } \begin{cases}\mathrm{LST}_{p2}\text{ is missing}\\ \text{can be filled with one}\\ \text{value}\end{cases}\\ \dfrac{\mathrm{LST}_{x_0,y_0,t2}+\mathrm{LST}_{x_0,y_0,t3}}{2}, & \text{if } \begin{cases}\mathrm{LST}_{p2}\text{ is missing}\\ \text{can be filled with two}\\ \text{values}\end{cases}\\ \mathrm{LST}_{p2}, & \text{if } \mathrm{LST}_{p2}\text{ is not missing}\end{cases} \tag{9}$$

where LST_{p3} is the predicted LST of the target pixel after temporal gapfilling; $\mathrm{LST}_{x_0,y_0,t1}$ is the LST at location (x_0, y_0)

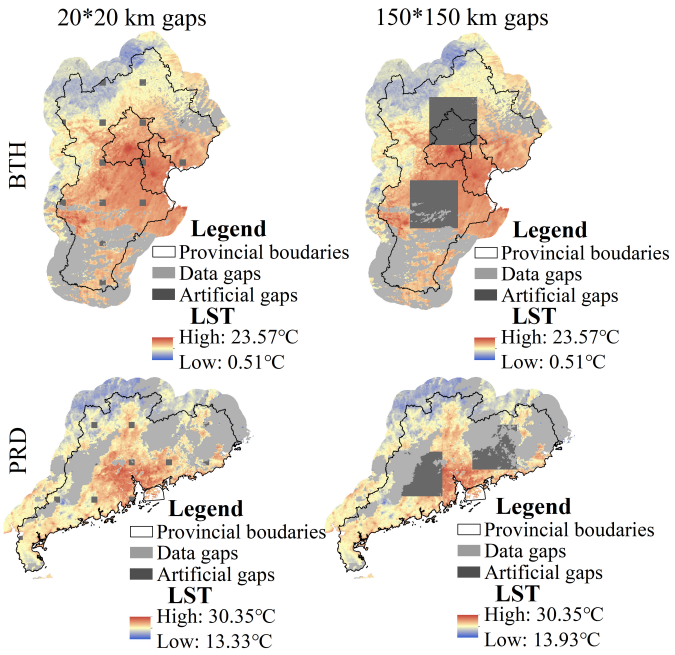

Fig. 3. Schematic diagrams of the introduced gaps in the LST images. MOD11 nighttime LST data from May 23, 2018, were used as examples. Pixels within 50 km of the periphery of the study area were retained to enable more spatial information to be used.

in the gapfilled image at day $t1$, which is the nearest date that has a valid LST; and $t2$ and $t3$ are the two equally nearby dates with valid LST values.

B. Accuracy Verification

In this study, gaps of 20 × 20 km and 150 × 150 km (representing small and large gaps, respectively) were artificially created in the original LST data on the eighth and twenty-third days of each month in 2018 (a total of 24 days) (Fig. 3). These artificial gaps were then filled with the method proposed in this study. The filled LSTs were then compared with the original observed LSTs. The mean absolute error (MAE) and root-mean-square error (RMSE) were calculated to describe the accuracy [8], [17], [20], [50].

C. Accuracy Comparison

The impact of some thresholds in the EH method should be analyzed in detail. A total of five thresholds were selected: 1) the number of preceding and following days with data used to remove outliers [in step (1)]; 2) the temperature threshold used to remove outliers [in step (1)]; 3) the number of preceding and following days with data used to fill the gaps [in step (2)]; 4) the initial window size used to fill the gaps in step (3)]; and 5) the maximum window size used to fill the gaps [in step (3)]. These thresholds were systematically analyzed in Supplementary Material 1.

Some settings for the EH method should be tested and discussed. First, the accuracies of the EH method with and without the removal of outliers [step (1)] were compared. Second, the effects of the three indexes [step (4)] on the accuracy of the EH method were analyzed. These settings were systematically analyzed in Supplementary Material 2.

The accuracy of the EH method was compared with three spatiotemporal gapfilling methods: Remotely Sensed DAily land Surface Temperature reconstruction (RSDAST) [19], interpolation of the mean anomalies (IMAs) [17], and Gapfill [42]. RSDAST first defines a spatiotemporal subset (similar to the EH method) for a missing LST and then fills the missing LST using (4). The filled LST is then considered a valid value when filling other pixels [19]. In the IMA method, a mean image of the subset is first calculated and then an anomaly image is computed, representing the LST difference between the target image and the mean image. Next, the gaps in the anomaly image are interpolated using the thin plate spine interpolation method. The final gapfilled image is calculated by adding the interpolated anomaly image to the mean image [17]. In the Gapfill method, a subset of images are first defined and then each image is ranked according to the proportion of values in the image that is the highest among members of the subset at the same location. Next, for images that have a valid value at the location of the target pixel, the quantile of this valid value relative to the entire image is calculated. Finally, all values in the prediction set are regressed using quantile regression, and the target pixel is predicted using fitted quantile regression [42].

These three methods were selected for two main reasons. First, it has been demonstrated that these methods have higher accuracy than do other gapfilling methods. For example, Liu *et al.* [27] found that the accuracy of RSDAST was higher than that of regression kriging interpolation. Militino *et al.* [17] found that the accuracy of IMA was higher than that of Gapfill, harmonic analysis of time series (HANTS) [51], and TIMESAT software. Gerber *et al.* [42] showed that the accuracy of the Gapfill method was higher than those of TIMESAT software and the spatiotemporal gapfilling method proposed by Weiss *et al.* [20]. Second, these methods can be easily implemented. RSDAST is relatively simple and does not require other auxiliary data. IMA and Gapfill can be easily implemented with the "RGISTool" and "Gapfill" add-on packages in R software, respectively. In addition, to reveal the effect of the information from other similar LST products on the accuracy, the accuracy of the EH method without the use of other LST products was calculated and compared with the original EH results. In this analysis, the subset members in step (2) were defined as the LST images from the same product as the target image in the four preceding and following days.

D. Real Examples

In addition to validating the accuracies of the gapfilling methods using artificial gaps, the performances of the gapfilling methods were evaluated for real examples. First, the gaps in the four daily LST products in 2018 were filled with the gapfilling methods. Second, the spatiotemporal variations in the gapfilled LST data were examined.

E. Calculation Costs

The calculation costs of the four methods were analyzed using the MOD11 daytime LST data from October 18, 2018, to October 28, 2018, in the BTH region and from October 27,

TABLE I

PROPORTIONS OF PIXELS WITH VALID VALUES OF THE FOUR PRODUCTS IN 2018. AT LEAST ONE: THE PROPORTIONS OF PIXELS WITH AT LEAST ONE VALID VALUE OF THE FOUR PRODUCTS

	MOD11	MYD11	MYD21	VNP21	At least one
The proportions of the pixels that have valid values in the BTH					
Daytime LST	46.5%	43.9%	39.8%	57.4%	66.3%
Nighttime LST	51.8%	53.5%	46.9%	64.4%	73.2%
The proportions of gaps that can be filled using information from other products in BTH					
Daytime LST	37.1%	40.0%	44.0%	20.9%	
Nighttime LST	44.3%	42.2%	49.4%	24.5%	
The proportions of pixels that have valid value in PRD					
Daytime LST	21.0%	21.0%	18.4%	30.9%	39.0%
Nighttime LST	22.7%	23.0%	19.6%	31.2%	42.2%
The proportions of gaps that can be filled using information from other products in PRD					
Daytime LST	22.8%	22.8%	25.3%	11.8%	
Nighttime LST	25.2%	24.9%	28.1%	15.9%	

2018, to November 7, 2018, in the PRD region. These dates were selected because their proportions of valid pixels to total pixels were evenly distributed between 0 and 1.

IV. RESULTS

A. Proportions of Valid Value

The proportions of the pixels that have valid values in 2018 are shown in Table I. The VNP21 product has the highest proportion of valid values because the swath width of the VIIRS sensor (3000 km) is significantly wider than that of the MODIS sensor (2330 km). Comparatively, the MYD21 product has the lowest proportion of valid values, which is primarily due to its stricter cloud removal method [49]. In Additionally, there are more missing values in the LST products for the PRD region than for the BTH region. The reason for this phenomenon is that the climate of PRD is more humid than that of BTH. Finally, the proportions of pixels that had at least one valid value in the four products were 66.3% (39.0%) and 73.2% (42.2%) for daytime and nighttime LSTs, respectively, for BTH (PRD).

The proportions of gaps that could be filled using information from other products are shown in Table I. Information from other products was more useful for the VNP21 product than for the other products. This is because the proportions of valid values in VNP21 were significantly higher than those in other products. Additionally, information from other products was more useful for BTH than for PRD. The reason for this is that the proportions of valid values for BTH were significantly higher than those for PRD.

B. Strong Correlations Between Different LST Products

The spatial correlations between the LST values of different products on the same day were compared with the spatial correlations between the LST values of the same product on two adjacent days. The spatial correlations between different LST products were calculated for 365 days in 2018. The spatial correlations between the same LST product on two adjacent days were calculated for 364 cases in 2018. The average coefficient of determination (R^2) of these correlations is shown in Fig. 4. It was found that the correlations between different LST products on the same day were stronger than

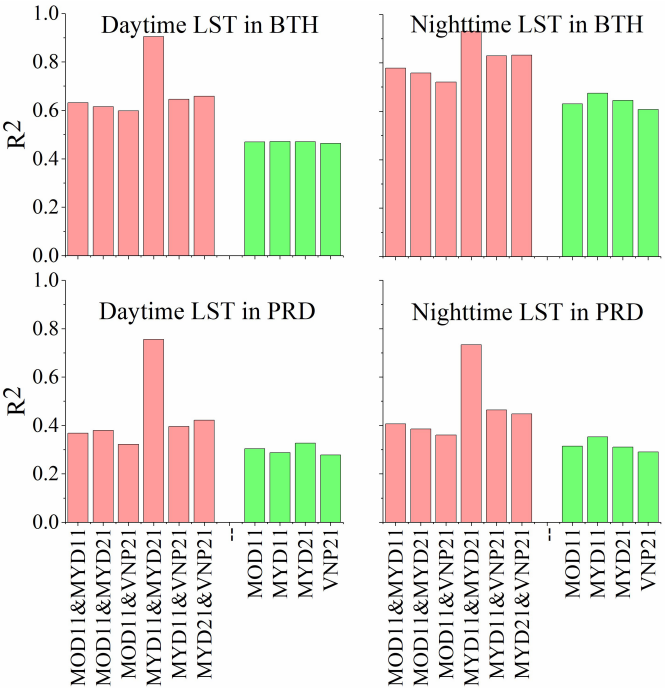

Fig. 4. Comparisons of the spatial correlations between different LST products and between the same LST product on two adjacent days. Red bars represent the spatial correlations between different LST products, averaged for 365 days. Green bars represent the spatial correlations between the same LST product on two adjacent days, averaged for 364 cases.

those between the same LST product on two adjacent days. For example, R^2 of the spatial correlations between different daytime LST products, averaged for 365 days for the BTH region, ranged from 0.598 to 0.905, while R^2 of the spatial correlations between the same LST product on two adjacent days, averaged for 364 cases, ranged from 0.464 to 0.471. These results suggested that using information gathered from other products on the same day to fill gaps may be more accurate than using information from the same product on adjacent days. This is primarily because the monitoring times of the four LST products are nearly the same. Additionally, the correlations between the MYD11 and MYD21 LST products were much stronger than those between the other LST products. This can be attributed to the fact that the MYD11 and MYD21 products are retrieved from the same raw data.

C. Accuracy of the Four Methods

The accuracies of the four gapfilling methods are shown in Tables II and III. The EH method significantly outperformed the three other methods. When filling 20 × 20-km gaps in daytime (nighttime) LST data, the average MAEs of the EH, RSDAST, IMA, and Gapfill methods were 0.845 (0.584) °C, 1.107 (0.791) °C, 1.316 (0.927) °C, and 1.374 (1.101) °C, respectively (Table II). When filling 150 × 150-km gaps in the daytime (nighttime) LST images, the average MAEs of the EH, RSDAST, IMA, and Gapfill methods were 1.031 (0.805) °C, 2.181 (1.573) °C, 1.596 (1.329) °C, and 1.860 (1.513) °C, respectively, (Table III). Therefore, the MAEs of the EH method were 23.7%–52.7% lower than those of RSDAST, 35.4%–38.7% lower than those of IMA, and 38.5%–46.9% lower than those of the Gapfill method. In addition, the

TABLE II

ACCURACIES OF FOUR GAPFILLING METHODS IN FILLING 20 × 20-KM GAPS. THE ACCURACIES FOR DAYTIME AND NIGHTTIME LSTS ARE PLACED AT THE LEFT AND RIGHT, RESPECTIVELY. UNIT: °C

		MOD11	MYD11	MYD21	VNP21	Average
BTH						
MAE	EH	0.704, 0.510	0.703, 0.423	0.800, 0.479	1.274, 0.793	0.870, 0.551
	RSDAST	0.844, 0.602	0.992, 0.638	1.182, 0.745	1.404, 0.916	1.106, 0.725
	IMA	0.995, 0.703	1.152, 0.700	1.376, 0.849	1.458, 0.947	1.245, 0.800
	Gapfill	1.180, 1.011	1.403, 0.974	1.598, 1.044	1.783, 1.196	1.491, 1.056
RMSE	EH	1.074, 0.722	1.169, 0.609	1.226, 0.713	1.878, 1.113	1.337, 0.789
	RSDAST	1.272, 0.850	1.544, 0.909	1.755, 1.069	2.079, 1.265	1.663, 1.023
	IMA	1.412, 0.974	1.676, 0.952	1.954, 1.337	2.109, 1.294	1.788, 1.139
	Gapfill	1.696, 1.390	1.999, 1.314	2.248, 1.448	2.500, 1.591	2.111, 1.436
PRD						
MAE	EH	0.624, 0.455	0.577, 0.475	0.704, 0.601	1.370, 0.936	0.819, 0.617
	RSDAST	0.740, 0.593	0.919, 0.669	1.106, 0.924	1.668, 1.244	1.108, 0.858
	IMA	1.105, 0.762	1.156, 0.853	1.488, 1.179	1.799, 1.424	1.387, 1.055
	Gapfill	0.939, 0.891	1.118, 1.004	1.273, 1.265	1.700, 1.421	1.258, 1.145
RMSE	EH	0.875, 0.688	0.841, 0.764	0.999, 1.006	2.055, 1.454	1.193, 0.978
	RSDAST	1.087, 1.025	1.548, 0.993	1.743, 1.454	2.538, 1.996	1.729, 1.367
	IMA	1.512, 1.031	1.560, 1.235	2.035, 1.662	2.530, 2.008	1.909, 1.484
	Gapfill	1.323, 1.270	1.553, 1.499	1.775, 1.903	2.403, 2.042	1.764, 1.679
Average						
MAE	EH	0.664, 0.483	0.640, 0.449	0.752, 0.540	1.322, 0.865	0.845, 0.584
	RSDAST	0.792, 0.598	0.956, 0.654	1.144, 0.835	1.536, 1.080	1.107, 0.791
	IMA	1.050, 0.733	1.154, 0.777	1.432, 1.014	1.629, 1.186	1.316, 0.927
	Gapfill	1.060, 0.951	1.261, 0.989	1.436, 1.155	1.742, 1.309	1.374, 1.101
RMSE	EH	0.975, 0.705	1.005, 0.687	1.113, 0.860	1.967, 1.284	1.265, 0.884
	RSDAST	1.180, 0.938	1.546, 0.951	1.749, 1.262	2.309, 1.631	1.696, 1.195
	IMA	1.462, 1.003	1.618, 1.094	1.995, 1.500	2.320, 1.651	1.849, 1.312
	Gapfill	1.510, 1.330	1.776, 1.407	2.012, 1.676	2.452, 1.817	1.937, 1.557

TABLE III

ACCURACIES OF FOUR GAPFILLING METHODS IN FILLING 150 × 150-KM GAPS. THE ACCURACIES OF DAYTIME AND NIGHTTIME LSTS ARE PLACED AT THE LEFT AND RIGHT, RESPECTIVELY. UNIT: °C

		MOD11	MYD11	MYD21	VNP21	Average
BTH						
MAE	EH	1.006, 0.723	0.888, 0.572	0.963, 0.602	1.549, 1.033	1.102, 0.733
	RSDAST	2.176, 1.224	2.476, 1.247	2.439, 1.428	2.818, 1.636	2.477, 1.384
	IMA	1.264, 1.045	1.524, 1.089	1.753, 1.135	1.754, 1.379	1.574, 1.162
	Gapfill	1.644, 1.331	1.985, 1.283	2.082, 1.362	2.261, 1.520	1.993, 1.374
RMSE	EH	1.540, 1.008	1.464, 0.820	1.488, 0.819	2.264, 1.477	1.689, 1.031
	RSDAST	3.196, 1.661	3.851, 1.675	3.687, 1.925	4.165, 2.308	3.725, 1.892
	IMA	1.751, 1.409	2.158, 1.581	2.500, 1.655	2.480, 1.961	2.222, 1.652
	Gapfill	2.380, 1.811	2.814, 1.727	2.912, 1.801	3.095, 2.085	2.800, 1.856
PRD						
MAE	EH	0.768, 0.688	0.643, 0.674	0.751, 0.854	1.683, 1.371	0.961, 0.897
	RSDAST	1.432, 1.353	1.672, 1.153	1.612, 2.056	2.822, 2.489	1.885, 1.763
	IMA	1.273, 1.128	1.277, 1.188	1.649, 1.675	2.271, 1.996	1.618, 1.497
	Gapfill	1.462, 1.296	1.524, 1.416	1.762, 1.824	2.160, 2.071	1.727, 1.652
RMSE	EH	1.079, 1.018	0.941, 1.065	1.080, 1.297	2.466, 2.056	1.392, 1.359
	RSDAST	1.960, 1.943	2.451, 1.573	2.596, 3.287	4.539, 4.020	2.887, 2.706
	IMA	1.748, 1.530	1.813, 1.612	2.732, 8.524	3.087, 2.715	2.345, 3.595
	Gapfill	2.153, 1.778	2.065, 2.134	2.592, 2.560	2.957, 3.009	2.442, 2.370
Average						
MAE	EH	0.887, 0.706	0.766, 0.623	0.857, 0.728	1.616, 1.202	1.031, 0.815
	RSDAST	1.804, 1.289	2.074, 1.200	2.026, 1.742	2.820, 2.063	2.181, 1.573
	IMA	1.269, 1.087	1.401, 1.139	1.701, 1.405	2.013, 1.688	1.596, 1.329
	Gapfill	1.553, 1.314	1.755, 1.350	1.922, 1.593	2.211, 1.796	1.860, 1.513
RMSE	EH	1.310, 1.013	1.203, 0.943	1.284, 1.058	2.365, 1.767	1.540, 1.195
	RSDAST	2.578, 1.802	3.151, 1.624	3.142, 2.606	4.352, 3.164	3.306, 2.299
	IMA	1.750, 1.470	1.986, 1.597	2.616, 5.090	2.784, 2.338	2.284, 2.623
	Gapfill	2.267, 1.795	2.440, 1.931	2.752, 2.181	3.026, 2.547	2.621, 2.113

MAEs obtained when the EH method was used to fill 20 × 20-km gaps in daytime and nighttime LST data were, on average, 0.845 °C and 0.584 °C, respectively. These accuracies are similar to the accuracies obtained for the MOD11 and MYD11 LST products themselves (< 1 °C in most cases [48], [52]). Furthermore, the EH method significantly outperformed the three other gapfilling methods for both BTH and PRD. These results suggest that the EH method performs well over the two study areas.

The primary reason for the high accuracy of the EH method is that it uses three kinds of information (spatial information, temporal information, and information from other

TABLE IV

ACCURACY OF THE EH METHOD WITHOUT THE USE OF INFORMATION FROM OTHER LST PRODUCTS. THE ACCURACIES OF DAYTIME AND NIGHTTIME LSTS ARE PLACED AT THE LEFT AND RIGHT, RESPECTIVELY. UNIT: °C

		MOD11	MYD11	MYD21	VNP21	Average
20 × 20 km gaps						
MAE	BTH	0.764, 0.563	0.929, 0.583	1.094, 0.691	1.301, 0.863	1.022, 0.675
	PRD	0.642, 0.502	0.758, 0.609	0.978, 0.844	1.472, 1.040	0.963, 0.749
	Average	0.703, 0.533	0.844, 0.596	1.036, 0.768	1.387, 0.952	0.992, 0.712
RMSE	BTH	1.142, 0.788	1.454, 0.808	1.628, 0.977	1.910, 1.186	1.534, 0.940
	PRD	0.915, 0.738	1.085, 0.899	1.383, 1.303	2.164, 1.543	1.387, 1.121
	Average	1.029, 0.763	1.270, 0.854	1.506, 1.140	2.037, 1.365	1.460, 1.030
150 × 150 km gaps						
MAE	BTH	1.130, 0.822	1.291, 0.851	1.434, 0.958	1.658, 1.182	1.378, 0.953
	PRD	0.831, 0.759	0.907, 0.902	1.068, 1.210	1.851, 1.499	1.164, 1.093
	Average	0.981, 0.791	1.099, 0.877	1.251, 1.084	1.755, 1.341	1.271, 1.023
RMSE	BTH	1.675, 1.128	1.989, 1.165	2.141, 1.281	2.400, 1.642	2.051, 1.304
	PRD	1.158, 1.085	1.284, 1.295	1.530, 1.710	2.641, 2.163	1.653, 1.563
	Average	1.417, 1.107	1.637, 1.230	1.836, 1.496	2.521, 1.903	1.852, 1.434

LST products), while RSDAST, IMA, and Gapfill use only spatial and temporal information. The accuracy of the EH method decreased significantly when information from other LST products was not used (Table IV). For example, when the 20 × 20-km gaps in the daytime and nighttime LST data were filled without the use of other LST products, the MAEs were, on average, 0.992 °C and 0.712 °C, respectively (Table IV). Comparatively, these values were 0.845 °C and 0.584 °C when other LST products were used (Table II). These results suggest that the usage of other LST products is the main reason for the high accuracy of the EH method. This can be explained by the fact that the four LST products used in this study have the same or nearly the same monitoring times. Therefore, the correlations between these products are strong, and the gaps can be accurately filled when information from other LST products is used.

In addition to the high accuracy of the EH method, three main results need to be mentioned. First, the accuracies of the four methods obtained when filling gaps in daytime LSTs were generally lower than those obtained when filling gaps in nighttime LSTs. This is mainly because daytime LSTs are more variable than are nighttime LSTs [16], which makes daytime LSTs hard to predict. Second, the accuracies of the four methods obtained when filling 20 × 20-km gaps were higher than those obtained when filling 150 × 150-km gaps. These results were logical since the 150 × 150-km gaps were filled using information from distant pixels. Third, the accuracies of the four gapfilling methods obtained when filling the VNP21 products were generally lower than those obtained when filling the MODIS products. The reason for this phenomenon is not clear but may be related to the differences in the spatial resolutions between the MODIS (1 km) and VIIRS sensors (750 m). The VNP21 LST product was released recently and has been used by few studies. More detailed analyses of this phenomenon should be performed in future studies.

D. Real Examples

The spatial distributions of the annual mean gapfilled LSTs in 2018 are presented in Figs. 5 and 6. The regional means and standard deviations of the annual mean gapfilled LSTs are shown in Table V. The EH, RSDAST, and IMA methods were used in this section. The Gapfill method was not selected because: 1) Gapfill is very time-consuming, especially for filling large gaps in daily LST products (see Section IV-E) and 2) Gapfill has a lower accuracy than do other gapfilling methods (see Section IV-C). The LSTs of the study areas were strongly dependent on elevation, with higher LST values in areas with lower elevations. The daytime LSTs of MYD11 were generally higher than those of MOD11, while the nighttime LSTs of MYD11 were normally lower than those of MOD11. These differences are primarily because the observation time of MYD11 is closer to the time of the appearance of the highest and lowest LSTs in the diurnal cycle than the observation time of MOD11 is. In addition, the LSTs of MYD21 and VNP21 were commonly higher than those of MYD11, although their monitoring times were the same. This can be explained by the following: 1) in arid areas, MYD21 and VNP21 corrected the cold bias of the MOD11 and MYD11 products and 2) in vegetated areas and water surfaces, MYD21 and VNP21 overestimated LSTs, but MOD11 and MYD11 underestimates LSTs [49], [53].

The LSTs filled by RSDAST were generally lower than those filled using the EH method (Figs. 5 and 6, Table V). Further analysis showed that this can partly be attributed to the extremely low values caused by undetected clouds. The EH method removed these outliers, but the RSDAST method did not. Additionally, the difference in LST data filled by the EH and IMA methods was primarily due to the IMA method generating some outliers when filling the missing LSTs.

Fig. 7 shows the temporal variations in the regional average LST after gapfilling. The LSTs were higher in summer and lower in winter. The LSTs filled by RSDAST were lower than those filled with the EH method on some days because the EH method removed extremely low LSTs due to undetected clouds. Additionally, there were some outliers in the LST curves filled with RSDAST and IMA. For example, the regional average LST was lower than 0°C on some days in the warm months. These results suggested that the EH method was more reliable than RSDAST and IMA in the real example. In addition, there were more outliers observed in the temporal variations in LSTs filled with RSDAST and IMA in PRD than were observed in BTH. This is probably because: 1) the ranges of LSTs in BTH were larger than those in PRD and 2) the

TABLE V

REGIONAL MEANS AND STANDARD DEVIATIONS OF ANNUAL MEAN GAPFILLED LSTS. UNIT: °C

Region	Method	MOD11	MYD11	MYD21	VNP21
Daytime					
BTH	EH	16.82±3.37	18.70±3.59	20.47±4.10	19.64±4.08
	RSDAST	16.23±3.18	17.42±3.23	18.20±3.82	18.09±3.97
	IMA	16.01±3.08	17.95±3.36	19.14±3.93	18.76±3.87
PRD	EH	23.68±2.00	25.39±2.22	28.88±2.79	27.12±2.80
	RSDAST	23.13±1.84	23.92±2.06	26.38±2.56	25.59±2.60
	IMA	23.95±2.29	24.28±2.22	27.69±3.13	26.51±3.76
Nighttime					
BTH	EH	4.12±3.53	2.87±3.58	4.30±3.89	3.74±3.87
	RSDAST	3.64±3.41	2.89±3.63	4.52±3.95	3.13±3.69
	IMA	3.81±3.43	2.74±3.69	3.99±4.06	3.47±3.78
PRD	EH	16.72±1.62	15.93±1.73	17.75±2.20	17.14±2.28
	RSDAST	15.25±1.43	14.90±1.69	16.20±2.13	15.77±2.25
	IMA	16.07±1.54	15.48±1.94	17.70±2.59	16.24±2.86

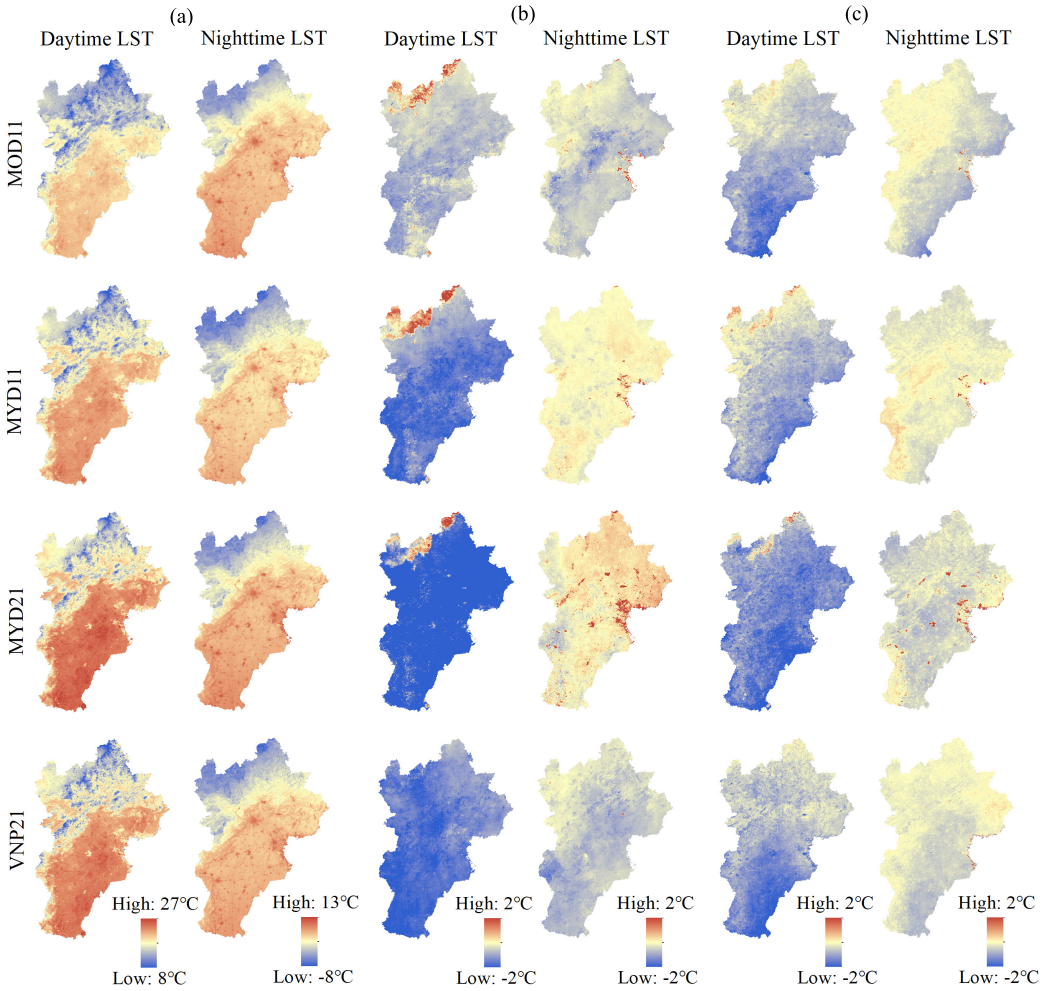

Fig. 5. Spatial distributions of the annual mean gapfilled LSTs in BTH in 2018. (a) EH, (b) RSDAST minus EH, (c) IMA minus EH.

proportions of missing values in the original LST products in PRD were higher than those in BTH, which makes it more challenging to fill the gaps in PRD.

E. Calculation Costs

The calculation costs of the four methods are shown in Table VI. The processing time of the gapfill method was the highest, followed by the IMA, EH, and RSDAST methods. The high processing time of the Gapfill method is because the ranking process is very time-consuming [17], [42]. The high processing time of IMA can be attributed to the usage of the thin plate spline interpolation method [17]. It should be noted that the processing time of IMA decreased when the number of missing values increased. This is because the processing time of the thin plate spline interpolation method decreased when the number of missing values increased. The reason for the higher processing time of the EH method than that of RSDAST is that: 1) the EH method uses information from other LST products, while RSDAST does not, and 2) RSDAST uses the filled LSTs to fill the next gap, while the EH method does not.

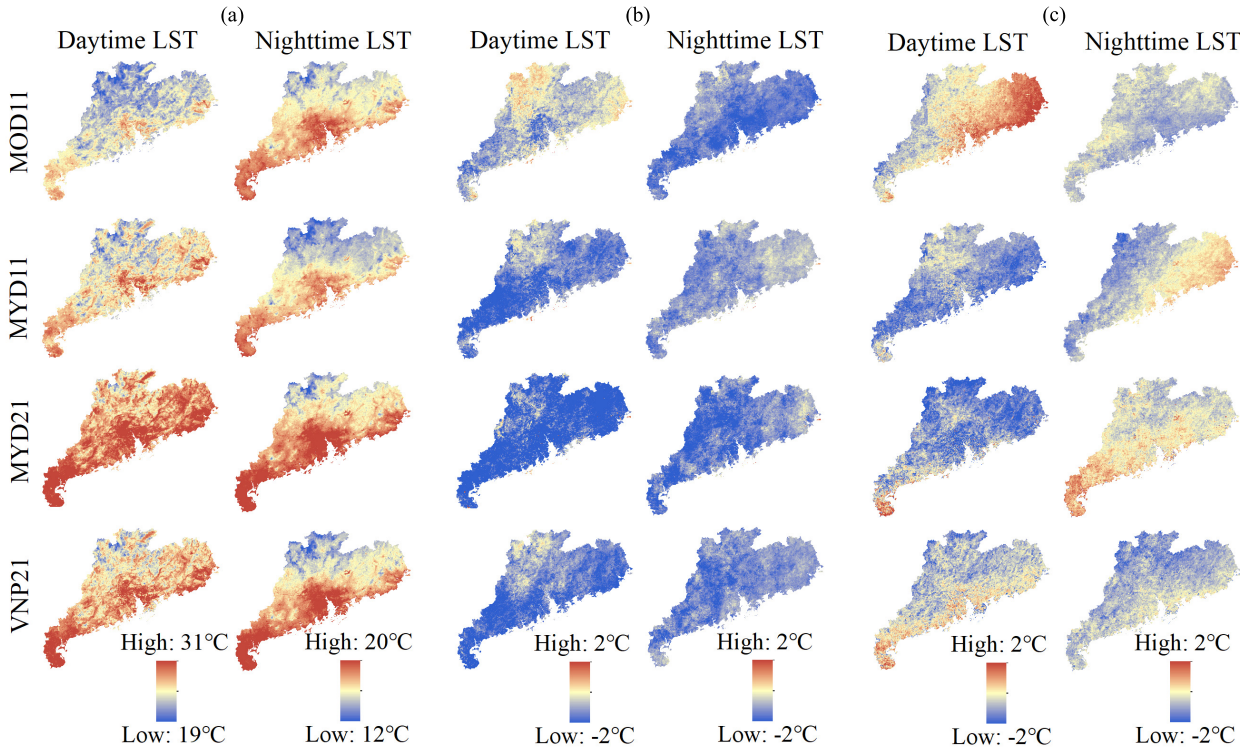

Fig. 6. Spatial distributions of the annual mean gapfilled LSTs in PRD in 2018. (a) EH, (b) RSDAST minus EH, and (c) IMA minus EH.

V. Discussion

A. Strengths

The EH method proposed in this study has several advantages, which are summarized as follows. The major advantage of the EH method is that it has a high accuracy compared with other gapfilling methods. The reason for the high accuracy of the EH method is that it can make full use of three kinds of information (i.e., spatial information, temporal information, and information from other LST products), while the IMA and Gapfill methods as well as most previous methods use only spatiotemporal information. The four LST products used in this study had similar spatiotemporal characteristics since their monitoring times were the same or nearly the same. Therefore, the usage of other similar products can improve the accuracy of gapfilling. The accuracy of the Gapfill method was low because it was originally developed to fill gaps in MODIS normalized difference vegetation index (NDVI) data [42], although it can be and has been used to fill gaps in LST data [8], [31]. The rank method in Gapfill works when filling gaps in NDVI data because images with high NDVIs generally indicate good atmospheric conditions [54]. However, this method may not work when filling LST data. The accuracy of IMA was relatively low because: 1) the calculation of the mean image has some uncertainties because there are numerous gaps in the original LST images. 2) To reduce computing costs, IMA uses a moving window average method to smooth the anomaly images. The accuracy of RSDAST was relatively low because this method uses the filled LSTs to fill the next gap [19]. This causes errors to propagate, especially for large gaps.

The EH method can fill all gaps in LST data, even if the LSTs are missing for the entire study area. This is because the EH method includes a temporal gapfilling step. In addition, the input data for the EH method are only the LST data; other auxiliary data are not required. The four LST data sets used in the EH method have global coverage and are freely available. Therefore, this method can be easily applied to any region of the world, although some modifications may be needed (e.g., to the outlier detection method). Finally, the EH method uses spatiotemporal information and other similar products to fill gaps in LST data. It can also be used to fill gaps in other satellite data sets that have spatiotemporal coherence and several similar products (e.g., sea surface temperature, vegetation index, snow cover, and aerosol optical depth data).

B. Limitations

The EH method proposed in the present study has three main limitations:

1) The reconstruction of LSTs can be divided into clear- and cloudy-sky LSTs. Both clear- and cloudy-sky LSTs are useful for the remote sensing community but have some limitations. Reconstructed clear-sky LST data have successfully been used in many research fields [28]–[32]. In addition, the estimation of clear-sky LSTs is an important step in some methods for estimating cloudy-sky LSTs [23], [33], [34]. However, reconstructed clear-sky LSTs are higher than real LSTs under cloudy-sky conditions. Reconstructed clear-sky LSTs cannot be used (or should be modified) in studies requiring real LSTs and may cause uncertainties

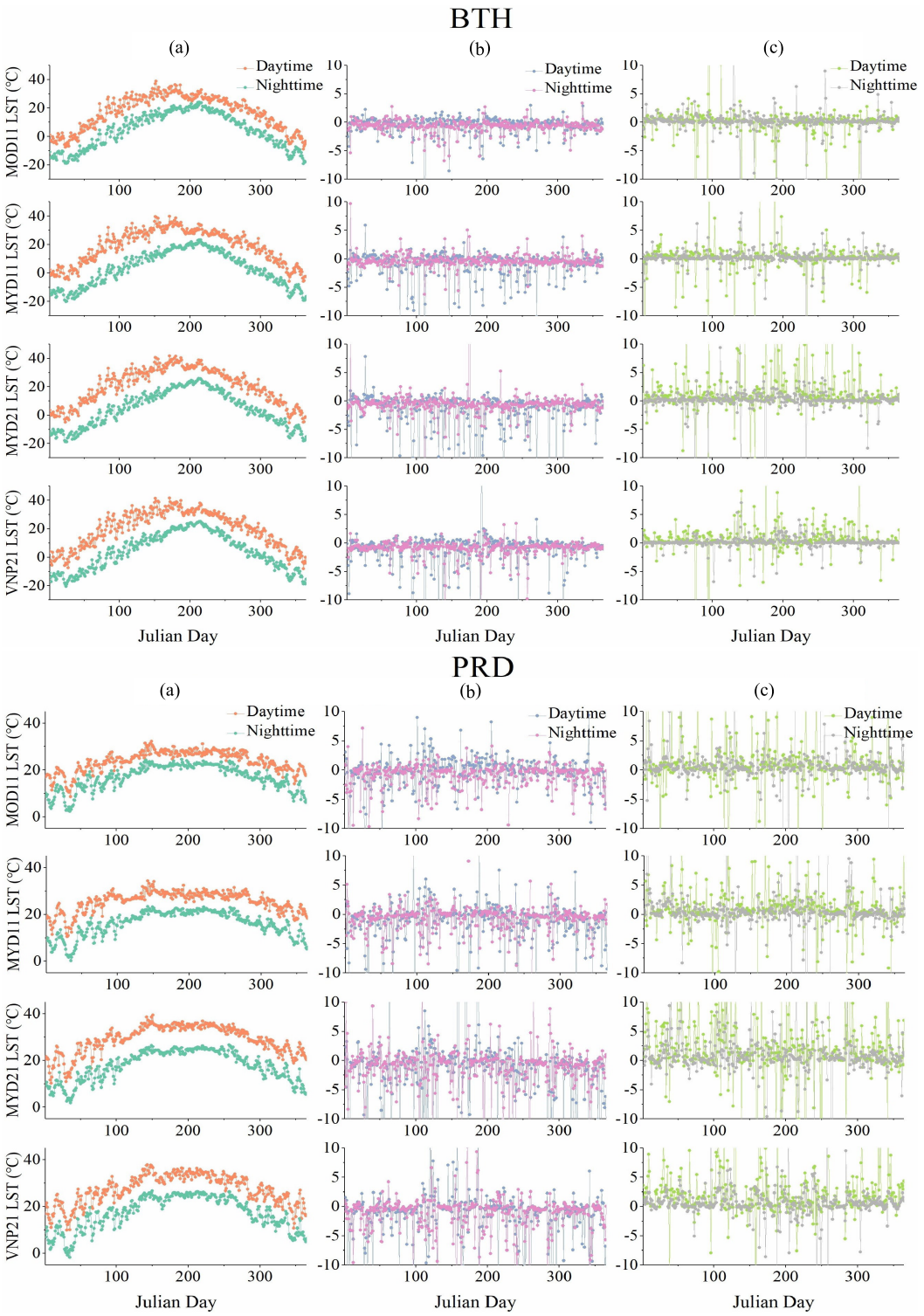

Fig. 7. Temporal variations in the regional average gapfilled LSTs. (a) EH, (b) RSDAST minus EH, and (c) IMA minus EH.

in some research fields (e.g., estimations of air temperature). Cloudy-sky LSTs are critical for studies of energy balance and water cycle [26]. However, the reconstruction of real LSTs under cloudy-sky conditions can be problematic and model-dependent. The accuracy of reconstructed cloudy-sky LSTs is lower than that of the reconstructed clear-sky LSTs [8], [17]–[21], [23]–[27]. The same as many previous studies [8], [17]–[21], [36]–[39], the only purpose of this article is to reconstruct clear-sky LSTs. The EH method could not be directly used in studies requiring real LSTs (e.g., studies estimating sensible and latent heat fluxes [26]). We are considering reconstructing clear-sky LSTs in the future. For example, similar to the approach

TABLE VI

PROCESSING TIMES OF THE FOUR GAPFILLING METHODS. PROPORTIONS OF VALID PIXELS TO TOTAL PIXELS ARE SHOWN IN BRACKETS. *INDICATES THAT THE PROCESSING TIME WAS MORE THAN TWO DAYS. UNIT: SECONDS

	EH	RSDAST	IMA	Gapfill
BTH				
Removing outliers	66	0	0	0
October 18 (0.851)	14	4	1372	227
October 19 (0.614)	37	6	971	531
October 20 (0.212)	302	12	162	48122
October 21 (0.107)	667	14	63	*
October 22 (0.305)	258	10	371	34404
October 23 (0.996)	2	2	2245	6
October 24 (0.792)	21	4	1460	487
October 25 (0.021)	950	15	21	*
October 26 (0.668)	144	6	896	16959
October 27 (0.925)	6	2	1989	104
October 28 (0.454)	368	9	417	227
Temporal interpolation	4	0	0	0
Total time	2839	84	9967	*
PRD				
Removing outliers	111	0	0	0
October 27 (0.843)	25	4	889	761
October 28 (0.902)	47	3	959	2185
October 29 (0.997)	2	2	1295	5
October 30 (0.998)	2	2	1347	3
October 31 (0.691)	95	6	645	3741
November 1 (0.505)	223	8	299	*
November 2 (0.013)	522	15	28	*
November 3 (0.227)	443	11	125	82492
November 4 (0.092)	562	12	59	*
November 5 (0.382)	105	10	412	2687
November 6 (0.528)	154	8	385	10125
November 7 (0.283)	489	11	107	*
Temporal interpolation	5	0	0	0
Total time	2785	92	6550	*

proposed by Zeng *et al.* [23], we are considering first reconstructing the clear-sky LSTs for cloudy regions, and then correcting clear-sky LSTs to the cloudy-sky LSTs. Additionally, the data–model fusion framework proposed by Long *et al.* [35] can be used to generate LST under all-weather conditions. This new approach can improve the quality of remote sensing retrievals and spatial resolution of land surface modeling, without largely degrading the accuracies of remote sensing and modeling.

2) The VNP21 LST product is only available from January 2012 to the present. Therefore, in studies requiring LST data for long time series or in early years, the VNP21 LST product could not be used, and the EH method should be modified.
3) The EH method uses four products from the 15 days following the target date to fill in missing values. This is a drawback for many real-time applications.

VI. CONCLUSION

In this study, a method called the EH method that integrates spatiotemporal information and information from other LST products was proposed to reconstruct clear-sky LSTs. The accuracy of the EH method was compared with the accuracies of three spatiotemporal gapfilling methods. In addition, the performances of the gapfilling methods were evaluated using real examples. The results are summarized as follows.

The correlations between the LSTs obtained by different products on the same day were stronger than the correlations between the LSTs obtained by the same product on two adjacent days. In the simulation study, the EH method significantly outperformed the RSDAST, IMA, and Gapfill methods. The MAEs of the EH method were, on average, 23.7%–52.7% lower than those of RSDAST, 35.4%–38.7% lower than those of IMA, and 38.5%–46.9% lower than those of the Gapfill method. The high accuracy of the EH method can primarily be attributed to the usage of information from other LST products. The EH method also outperformed IMA in real examples. The LST images filled with RSDAST and IMA had some outliers, while there were fewer obvious outliers in the LST images filled with the EH method.

Overall, this study proposed a robust method that can be used to fill gaps in LST data. Future studies should: 1) use the EH method to fill gaps in LST data and then use the gapfilled LST data to investigate the surface urban heat island effect and develop a spatially continuous air temperature map; 2) analyze the accuracy of using the EH method to fill gaps in sea surface temperature, vegetation index, snow cover, and aerosol optical depth data; and 3) test the EH method on more climate and land cover types.

ACKNOWLEDGMENT

The authors would like to thank the Editors and the anonymous reviewers for their constructive comments and suggestions.

REFERENCES

[1] X. Huang, T. Hu, J. Li, Q. Wang, and J. A. Benediktsson, "Mapping urban areas in China using multisource data with a novel ensemble SVM method," *IEEE Trans. Geosci. Remote Sens.*, vol. 56, no. 8, pp. 4258–4273, Aug. 2018.
[2] R. Yao, L. Wang, X. Huang, W. Gong, and X. Xia, "Greening in rural areas increases the surface urban heat island intensity," *Geophys. Res. Lett.*, vol. 46, no. 4, pp. 2204–2212, Feb. 2019.
[3] R. Yao *et al.*, "Developing a temporally accurate air temperature dataset for Mainland China," *Sci. Total Environ.*, vol. 706, Mar. 2020, Art. no. 136037.
[4] D. Long *et al.*, "Generation of spatially complete and daily continuous surface soil moisture of high spatial resolution," *Remote Sens. Environ.*, vol. 233, Nov. 2019, Art. no. 111364.
[5] N. Lu *et al.*, "Hierarchical Bayesian space-time estimation of monthly maximum and minimum surface air temperature," *Remote Sens. Environ.*, vol. 211, pp. 48–58, Jun. 2018.
[6] L. Li and Y. Zha, "Satellite-based regional warming hiatus in China and its implication," *Sci. Total Environ.*, vol. 648, pp. 1394–1402, Jan. 2019.
[7] A. Bhardwaj *et al.*, "MODIS-based estimates of strong snow surface temperature anomaly related to high altitude earthquakes of 2015," *Remote Sens. Environ.*, vol. 188, pp. 1–8, Jan. 2017.
[8] X. Li, Y. Zhou, G. R. Asrar, and Z. Zhu, "Creating a seamless 1 km resolution daily land surface temperature dataset for urban and surrounding areas in the conterminous United States," *Remote Sens. Environ.*, vol. 206, pp. 84–97, Mar. 2018.
[9] J. Lai *et al.*, "Identification of typical diurnal patterns for clear-sky climatology of surface urban heat islands," *Remote Sens. Environ.*, vol. 217, pp. 203–220, Nov. 2018.
[10] X. Li, Y. Zhou, G. R. Asrar, M. Imhoff, and X. Li, "The surface urban heat island response to urban expansion: A panel analysis for the conterminous United States," *Sci. Total Environ.*, vols. 605–606, pp. 426–435, Dec. 2017.
[11] R. Yao, L. Wang, X. Gui, Y. Zheng, H. Zhang, and X. Huang, "Urbanization effects on vegetation and surface urban heat islands in China's Yangtze river basin," *Remote Sens.*, vol. 9, no. 6, p. 540, May 2017.
[12] L. Hu and N. A. Brunsell, "The impact of temporal aggregation of land surface temperature data for surface urban heat island (SUHI) monitoring," *Remote Sens. Environ.*, vol. 134, pp. 162–174, Jul. 2013.

[13] H. Zhang, F. Zhang, M. Ye, T. Che, and G. Zhang, "Estimating daily air temperatures over the Tibetan Plateau by dynamically integrating MODIS LST data," *J. Geophys. Res.-Atmos.*, vol. 121, no. 19, pp. 11425–11441, Oct. 2016.

[14] W. Zhu, A. Lú, and S. Jia, "Estimation of daily maximum and minimum air temperature using MODIS land surface temperature products," *Remote Sens. Environ.*, vol. 130, pp. 62–73, Mar. 2013.

[15] L. Shi, P. Liu, I. Kloog, M. Lee, A. Kosheleva, and J. Schwartz, "Estimating daily air temperature across the Southeastern United States using high-resolution satellite data: A statistical modeling study," *Environ. Res.*, vol. 146, pp. 51–58, Apr. 2016.

[16] C. Yoo, J. Im, S. Park, and L. J. Quackenbush, "Estimation of daily maximum and minimum air temperatures in urban landscapes using MODIS time series satellite data," *ISPRS J. Photogramm. Remote Sens.*, vol. 137, pp. 149–162, Mar. 2018.

[17] A. F. Militino, M. D. Ugarte, U. Perez-Goya, and M. G. Genton, "Interpolation of the mean anomalies for cloud filling in land surface temperature and normalized difference vegetation index," *IEEE Trans. Geosci. Remote Sens.*, vol. 57, no. 8, pp. 6068–6078, Aug. 2019.

[18] C. Zeng, H. Shen, M. Zhong, L. Zhang, and P. Wu, "Reconstructing MODIS LST based on multitemporal classification and robust regression," *IEEE Geosci. Remote Sens. Lett.*, vol. 12, no. 3, pp. 512–516, Mar. 2015.

[19] L. Sun *et al.*, "Reconstructing daily clear-sky land surface temperature for cloudy regions from MODIS data," *Comput. Geosci.*, vol. 105, pp. 10–20, Aug. 2017.

[20] D. J. Weiss, P. M. Atkinson, S. Bhatt, B. Mappin, S. I. Hay, and P. W. Gething, "An effective approach for gap-filling continental scale remotely sensed time-series," *ISPRS J. Photogramm. Remote Sens.*, vol. 98, pp. 106–118, Dec. 2014.

[21] H. T. Pham, S. Kim, L. Marshall, and F. Johnson, "Using 3D robust smoothing to fill land surface temperature gaps at the continental scale," *Int. J. Appl. Earth Observ. Geoinf.*, vol. 82, Oct. 2019, Art. no. 101879.

[22] W. Yu, J. Tan, M. Ma, X. Li, X. She, and Z. Song, "An effective similar-pixel reconstruction of the high-frequency cloud-covered areas of Southwest China," *Remote Sens.*, vol. 11, no. 3, p. 336, Feb. 2019.

[23] C. Zeng, D. Long, H. Shen, P. Wu, Y. Cui, and Y. Hong, "A two-step framework for reconstructing remotely sensed land surface temperatures contaminated by cloud," *ISPRS J. Photogramm. Remote Sens.*, vol. 141, pp. 30–45, Jul. 2018.

[24] G. Yang, W. Sun, H. Shen, X. Meng, and J. Li, "An integrated method for reconstructing daily MODIS land surface temperature data," *IEEE J. Sel. Topics Appl. Earth Observ. Remote Sens.*, vol. 12, no. 3, pp. 1026–1040, Mar. 2019.

[25] S.-B. Duan, Z.-L. Li, and P. Leng, "A framework for the retrieval of all-weather land surface temperature at a high spatial resolution from polar-orbiting thermal infrared and passive microwave data," *Remote Sens. Environ.*, vol. 195, pp. 107–117, Jun. 2017.

[26] H. R. Shwetha and D. N. Kumar, "Prediction of high spatio-temporal resolution land surface temperature under cloudy conditions using microwave vegetation index and ANN," *ISPRS J. Photogramm. Remote Sens.*, vol. 117, pp. 40–55, Jul. 2016.

[27] Z. Liu *et al.*, "Balancing prediction accuracy and generalization ability: A hybrid framework for modelling the annual dynamics of satellite-derived land surface temperatures," *ISPRS J. Photogramm. Remote Sens.*, vol. 151, pp. 189–206, May 2019.

[28] X. Liu, Y. Zhou, W. Yue, X. Li, Y. Liu, and D. Lu, "Spatiotemporal patterns of summer urban heat island in Beijing, China using an improved land surface temperature," *J. Cleaner Prod.*, vol. 257, Jun. 2020, Art. no. 120529.

[29] Y. Li, X. Wang, Y. Chen, and M. Wang, "Land surface temperature variations and their relationship to fractional vegetation coverage in subtropical regions: A case study in Fujian province, China," *Int. J. Remote Sens.*, vol. 41, no. 6, pp. 2081–2097, Mar. 2020.

[30] X. Li, Y. Zhou, G. R. Asrar, and Z. Zhu, "Developing a 1 km resolution daily air temperature dataset for urban and surrounding areas in the conterminous United States," *Remote Sens. Environ.*, vol. 215, pp. 74–84, Sep. 2018.

[31] R. I. Leihy, G. A. Duffy, E. Nortje, and S. L. Chown, "High resolution temperature data for ecological research and management on the southern ocean islands," *Sci. Data*, vol. 5, no. 1, Sep. 2018, Art. no. 180177.

[32] S. Yang, D. Zhang, L. Sun, Y. Wang, and Y. Gao, "Assessing drought conditions in cloudy regions using reconstructed land surface temperature," *J. Meteorol. Res.*, vol. 34, no. 2, pp. 264–279, Apr. 2020.

[33] Y. Zhang, Y. Chen, Y. Li, H. Xia, and J. Li, "Reconstructing one kilometre resolution daily clear-sky LST for China's landmass using the BME method," *Remote Sens.*, vol. 11, no. 22, p. 2610, Nov. 2019.

[34] T. Wang *et al.*, "Recovering land surface temperature under cloudy skies considering the solar-cloud-satellite geometry: Application to MODIS and Landsat-8 data," *J. Geophys. Res., Atmos.*, vol. 124, no. 6, pp. 3401–3416, Mar. 2019.

[35] D. Long *et al.*, "Generation of MODIS-like land surface temperatures under all-weather conditions based on a data fusion approach," *Remote Sens. Environ.*, vol. 246, Sep. 2020, Art. no. 111863.

[36] M. Neteler, "Estimating daily land surface temperatures in mountainous environments by reconstructed MODIS LST data," *Remote Sens.*, vol. 2, no. 1, pp. 333–351, Jan. 2010.

[37] J. Yang, Y. Wang, and P. August, "Estimation of land surface temperature using spatial interpolation and satellite-derived surface emissivity," *J. Environ. Inform.*, vol. 4, no. 1, pp. 37–44, Sep. 2004.

[38] L. Ke, X. Ding, and C. Song, "Reconstruction of time-series MODIS LST in central Qinghai-Tibet plateau using geostatistical approach," *IEEE Geosci. Remote Sens. Lett.*, vol. 10, no. 6, pp. 1602–1606, Nov. 2013.

[39] Y. Xu and Y. Shen, "Reconstruction of the land surface temperature time series using harmonic analysis," *Comput. Geosci.*, vol. 61, pp. 126–132, Dec. 2013.

[40] W. L. Crosson, M. Z. Al-Hamdan, S. N. J. Hemmings, and G. M. Wade, "A daily merged MODIS aqua–terra land surface temperature data set for the conterminous United States," *Remote Sens. Environ.*, vol. 119, pp. 315–324, Apr. 2012.

[41] N. C. Coops, D. C. Duro, M. A. Wulder, and T. Han, "Estimating afternoon MODIS land surface temperatures (LST) based on morning MODIS overpass, location and elevation information," *Int. J. Remote Sens.*, vol. 28, no. 10, pp. 2391–2396, May 2007.

[42] F. Gerber, R. D. Jong, M. E. Schaepman, G. Schaepman-Strub, and R. Furrer, "Predicting missing values in spatio-temporal remote sensing data," *IEEE Trans. Geosci. Remote Sens.*, vol. 56, no. 5, pp. 2841–2853, May 2018.

[43] A. F. Militino, M. D. Ugarte, and M. Montesino, "Filling missing data and smoothing altered data in satellite imagery with a spatial functional procedure," *Stochastic Environ. Res. Risk Assessment*, vol. 33, no. 10, pp. 1737–1750, Oct. 2019.

[44] W. Yu, Z. Nan, Z. Wang, H. Chen, T. Wu, and L. Zhao, "An effective interpolation method for MODIS land surface temperature on the Qinghai–Tibet plateau," *IEEE J. Sel. Topics Appl. Earth Observ. Remote Sens.*, vol. 8, no. 9, pp. 4539–4550, Sep. 2015.

[45] Z. Wan, "New refinements and validation of the collection-6 MODIS land-surface temperature/emissivity product," *Remote Sens. Environ.*, vol. 140, pp. 36–45, Jan. 2014.

[46] Z. Wan and J. Dozier, "A generalized split-window algorithm for retrieving land-surface temperature from space," *IEEE Trans. Geosci. Remote Sens.*, vol. 34, no. 4, pp. 892–905, Jul. 1996.

[47] G. Hulley, S. Veraverbeke, and S. Hook, "Thermal-based techniques for land cover change detection using a new dynamic MODIS multispectral emissivity product (MOD21)," *Remote Sens. Environ.*, vol. 140, pp. 755–765, Jan. 2014.

[48] Z. Wan, "New refinements and validation of the MODIS land-surface temperature/emissivity products," *Remote Sens. Environ.*, vol. 112, no. 1, pp. 59–74, Jan. 2008.

[49] R. Yao *et al.*, "A detailed comparison of MYD11 and MYD21 land surface temperature products in mainland China," *Int. J. Digit. Earth*, vol. 13, no. 12, pp. 1–17, Jan. 2020.

[50] W. Qin *et al.*, "Comparison of deterministic and data-driven models for solar radiation estimation in China," *Renew. Sustain. Energy Rev.*, vol. 81, pp. 579–594, Jan. 2018.

[51] G. J. Roerink, M. Menenti, and W. Verhoef, "Reconstructing cloudfree NDVI composites using Fourier analysis of time series," *Int. J. Remote Sens.*, vol. 21, no. 9, pp. 1911–1917, Jan. 2000.

[52] C. Coll, V. Garcia-Santos, R. Niclos, and V. Caselles, "Test of the MODIS land surface temperature and emissivity separation algorithm with ground measurements over a rice paddy," *IEEE Trans. Geosci. Remote Sens.*, vol. 54, no. 5, pp. 3061–3069, May 2016.

[53] N. K. Malakar and G. C. Hulley, "A water vapor scaling model for improved land surface temperature and emissivity separation of MODIS thermal infrared data," *Remote Sens. Environ.*, vol. 182, pp. 252–264, Sep. 2016.

[54] B. Wang *et al.*, "Vegetation dynamics and their relationships with climatic factors in the Qinling mountains of China," *Ecol. Indicators*, vol. 108, Jan. 2020, Art. no. 105719.

Rui Yao received the B.S. degree from Hubei University, Wuhan, China, in 2016. He is pursuing the Ph.D. degree with the China University in Geosciences, Wuhan, China.

His research interests include urban climate, thermal remote sensing, and satellite image processing.

Lunche Wang received the B.S. degree in geographic information system from Chuzhou University, Chuzhou, China, in 2010, and the M.S. and Ph.D. degrees in geography and photogrammetry and remote sensing from Wuhan University, Wuhan, China, in 2012 and 2015, respectively.

He is a Professor with the School of Earth Sciences, China University of Geosciences, Wuhan, China. His research interests include climate change and remote sensing of environment.

Xin Huang (Senior Member, IEEE) received the Ph.D. degree in photogrammetry and remote sensing from Wuhan University, Wuhan, China, in 2009.

He is with the State Key Laboratory of Information Engineering in Surveying, Mapping and Remote Sensing, Wuhan University, where he is also a Luojia Distinguished Professor and he teaches remote sensing, photogrammetry, and image interpretation. He is the Founder and the Director with the Institute of Remote Sensing Information Processing, School of Remote Sensing and Information Engineering, Wuhan University. He has authored over 130 peer-reviewed articles (SCI papers) in the international journals. His research interests include remote sensing image processing methods and applications.

Dr. Huang has been supported by The National Program for Support of Top-notch Young Professionals in 2017, the China National Science Fund for Excellent Young Scholars in 2015, and the New Century Excellent Talents in University from the Ministry of Education of China in 2011. He was a recipient of the Boeing Award for the Best Paper in Image Analysis and Interpretation from the American Society for Photogrammetry and Remote Sensing (ASPRS) in 2010, the second place recipient for the John I. Davidson President's Award from ASPRS in 2018, and the National Excellent Doctoral Dissertation Award of China in 2012. In 2011, he was recognized by the IEEE Geoscience and Remote Sensing Society (GRSS) as the Best Reviewer of the IEEE GEOSCIENCE AND REMOTE SENSING LETTERS. He was the Winner of the IEEE GRSS 2014 Data Fusion Contest. He was the Lead Guest Editor of the Special Issue on Information Extraction From High-Spatial-Resolution Optical Remotely Sensed Imagery for the IEEE JOURNAL OF SELECTED TOPICS IN APPLIED EARTH OBSERVATIONS AND REMOTE SENSING (vol. 8, no. 5, May 2015) and the Special Issue on Sparsity-Driven High Dimensional Remote Sensing Image Processing and Analysis for the *Journal of Applied Remote Sensing* (vol. 10, no. 4, Oct 2016). He has been serving as an Associate Editor for the Photogrammetric Engineering and Remote Sensing since 2016, the IEEE GEOSCIENCE AND REMOTE SENSING LETTERS since 2014, and the IEEE JOURNAL OF SELECTED TOPICS IN APPLIED EARTH OBSERVATIONSAND REMOTE SENSING since 2018. He has been an Editorial Board Member of Remote Sensing (an open access journal from MDPI) since 2018.

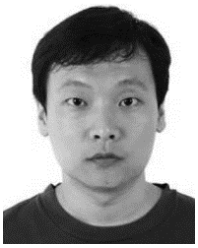

Liang Sun received the B.S. degree in land resources management from the China University of Geoscience, Beijing, China, in 2005, and the M.S. and Ph.D. degrees in remote sensing from the Beijing Normal University, Beijing, China, in 2007 and 2010, respectively.

His research interests include evapotranspiration, soil moisture, and agricultural remote sensing.

Ruiqing Chen received the B.S. degree in resources-environment and urban-rural planning management from Heilongjiang University of Science and Technology, Harbin, China, in 2015, and the M.S. degree in cartography and geography information system from Central China Normal University, Wuhan, China, in 2018. He is pursuing the Ph.D. degree in agriculture remote sensing from Chinese Academy of Agricultural Sciences, Beijing, China.

His research interests include early crop-type identification and remote sensing monitoring of agricultural conditions.

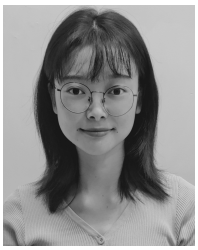

Xiaojun Wu received the B.S. degree in Guizhou Normal University, Guizhou, China, in 2018. She is currently pursuing the M.S. degree with the School of Geography and Information Engineering, China University of Geosciences, Wuhan, China.

Her research interests include climate change and extreme weather.

Wei Zhang received the B.S. degree in geographic information science from the Anhui Jianzhu University, Hefei, China, in 2018. She is pursuing the M.S. degree with the School of Geography and Information Engineering, China University of Geosciences, Wuhan, China.

Her research interests include climate change and vegetation remote sensing.

Zigeng Niu received the B.S. and M.S. degrees from China University in Geosciences, Wuhan, China, in 2015 and 2018, respectively. He is pursuing the Ph.D. degree with the China University of Geosciences, Wuhan, China.

His research interests include climate change and solar radiation.